Nanoscale

PAPER

Cite this: *Nanoscale*, 2020, **12**, 1842

Magnetic force fields of isolated small nanoparticle clusters†

C. Iacovita, [a,b] J. Hurst,[c] G. Manfredi, [a] P. A. Hervieux, [a] B. Donnio, [a] J. L. Gallani [a] and M. V. Rastei *[a]

Received 8th October 2019,
Accepted 19th December 2019

DOI: 10.1039/c9nr08634j

rsc.li/nanoscale

The usage of magnetic nanoparticles (NPs) in applications necessitates a precise mastering of their properties at the single nanoparticle level. There has been a lot of progress in the understanding of the magnetic properties of NPs, but incomparably less when interparticle interactions govern the overall magnetic response. Here, we present a quantitative investigation of magnetic fields generated by small clusters of NPs assembled on a dielectric non-magnetic surface. Structures ranging from individual NPs to fifth-fold particulate clusters are investigated in their magnetization saturation state by magnetic force microscopy and numerical calculations. It is found that the magnetic stray field does not increase proportionally with the number of NPs in the cluster. Both measured and calculated magnetic force fields underline the great importance of the exact spatial arrangement of NPs, shedding light on the magnetic force field distribution of particulate clusters, which is relevant for the quantitative evaluation of their magnetization and perceptibly for many applications.

1. Introduction

Stable and well characterized magnetic nanoparticles (NPs) are much sought after in many research fields. In particular, bio-related applications making use of iron-oxide NPs (magnetite – Fe_3O_4 and maghemite – Fe_2O_3) are currently one of the pharmaceutical markets with the fastest growth.[1,2] Such nanoparticles are now intensively used in biomedical imaging, diagnostic and therapeutic applications.[3–7] Their rather easy synthesis,[8–10] along with their peculiar magnetic properties[11] and relatively low toxicity[12,13] also make them ideal candidates as contrast agents for magnetic resonance imaging (MRI),[14–17] heat generators for cancer treatment by magnetic hyperthermia,[18–21] and carriers in drug delivery systems.[22,23] As always the case for any compound which is meant to be used in human health, there are stringent requirements on the properties of these materials. From the nanometer-scale interaction point of view, the magnetic properties of NPs are of utmost importance for their entire spectrum of applications.[24] For example, the local magnetic field surrounding the NPs is crucial for self-organization of NPs in solutions and on surfaces.[25,26] Or, the magnetic field of NPs is key for magnetic relaxation-based detection, which is not limited to MRI.[27] Magnetic relaxation-based detection exploits the local magnetic field generated by NPs by altering the spin–spin relaxation time of nearby molecules. In the MRI detection scheme the additional homogeneous external magnetic field is high enough to enable a magnetization saturation state of NPs. In any case, the study of NPs in their magnetic saturation state is consequently of critical importance.

The local magnetic field is nonetheless strongly modified by aggregation, an effect which has been recognized quite early to further enhance the rate of transverse spin relaxation of nearby water molecules for instance.[27–30] An efficient implementation of NPs in applications is consequently strongly related not only to their saturation magnetization – an active research field in synthetic inorganic chemistry – but also to the magnetic properties of NPs, which has been shown to be impacted by the degree of clustering,[22,31–35] or the formation of controlled multicore particulate architectures.[36–38] The characterization of the local magnetic field generated by either individual or few interacting NPs (hereafter referred to as clusters) is, therefore, also of great interest.

Here, we present an experimental and theoretical study on a quantitative evaluation of the magnetic force fields created by clusters consisting of 1 to 5 NPs. A homogeneous external magnetic field able to saturate the magnetization of NPs has been used. It was found that the local magnetic force fields do

[a]*Institut de Physique et Chimie des Matériaux de Strasbourg, CNRS, Université de Strasbourg, F-67034 Strasbourg, France. E-mail: rastei@ipcms.unistra.fr; Tel: +33 38810 7158*

[b]*Department of Pharmaceutical Physics-Biophysics, Faculty of Pharmacy, "Iuliu Hatieganu" University of Medicine and Pharmacy, Pasteur 6, 400349 Cluj-Napoca, Romania*

[c]*Department of Physics and Astronomy, Uppsala University, P. O. Box 516, SE-75120 Uppsala, Sweden*

†Electronic supplementary information (ESI) available. See DOI: 10.1039/C9NR08634J

not increase proportionally with the number of NPs in the clusters. Moreover, minute modifications of the spatial arrangement of NPs in the cluster were found to drastically modify the magnetic stray field, which in turn has a great impact on the quantitative determination of the magnetic moments of the clusters. In particular, it is shown that at distances smaller than the size of the clusters, the NPs do not equally contribute to the measured signal, yielding an overestimation of the magnetic moment of clusters when using a two-dipole model. This model is nevertheless shown to be suited for distances exceeding some critical values, which can be roughly approximated as twice the diameter of NPs forming the clusters. For measurements performed at larger distances, the application of the two-dipole model leads to a good estimation of the magnetic moments, improving further for clusters having a compact configuration.

Our numerical analyses were carried out by virtually splitting both the tip and the clusters into a large number of microscopic elements, permitting a full pairwise integration of magnetostatic potentials. This method allows taking into account the exact geometry of both tip and sample, which is crucial in the present study. Using the numerical results given by our model in combination with the experimental findings, we provide unprecedented insight into the quantitative evaluation of the magnetic field generated by the clusters of NPs. The importance of the tip–sample distance and of the spatial organization of the particulate clusters is clearly emphasized. The results shed light on the magnetic force field distribution near the clusters of NPs, which is relevant for a broad range of applications.

2. Experimental and modeling details

The investigation of the local field distribution above magnetic nanostructures of dimensions down to a few nanometers can be experimentally achieved by means of either magnetic force microscopy (MFM)[39] or electron holography.[40] The former technique has been extensively used in the last two decades and is now a mature approach, providing unique information about the nanoscale magnetism of on-surface,[41,42] immersed[43] or embedded nanostructures.[44] MFM uses the attractive and/or repulsive magnetostatic interactions established between the magnetic probe of the microscope and the near-field magnetic stray field emerging from the nanostructure, yielding a force gradient image. The signal is generally measured by converting the local magnetostatic interaction to an amplitude or phase change of the vibrating cantilevered MFM tip.[39,41] In a first approximation, the phase shift of the cantilever vibration can be written as a function of the gradient force along the z-direction:

$$\Delta\phi = -\frac{Q}{k}\frac{\partial F_z}{\partial z}, \quad (1)$$

where Q is the oscillation quality factor of the cantilever and k is the cantilever spring constant. For quantitative information, the phase shift needs to be probed at various tip–sample distances. This is in order to allow a 3D imaging of the magnetic field distribution generated by the magnetic nanostructure.[39,45] Moreover, a quantitative interpretation of the phase shift is also complex, since it depends on the detailed magnetic properties of the tip.[46,47] A few experimental studies have nevertheless proven the extraction of quantitative information feasible, such as magnetization or coercive fields, provided the exact spatial distribution of the tip magnetization is known.[48–51] Nonetheless, in many studies the two-dipole model[52] was used to interpret the experimental findings.[53–55]

The two-dipole model, also called the point-probe model, replaces the magnetic nanostructure by a unique magnetic dipole moment, and idealizes the tip magnetization by a magnetic dipole moment which is virtually located in the tip at a certain distance from the apex.[52] Within this model, the phase shift of the cantilever is directly proportional to the nanostructure magnetic dipole moment and to the magnetic dipole moment of the tip.[52] This two-dipole model has been successfully applied for extracting quantitative magnetic information, particularly on nanostructures able to generate field geometries similar to those used for the tip calibration.[56–58] Accordingly, spherical NPs with known magnetization have been employed to calibrate the magnetic tips, which were subsequently used to determine the magnetic moment of other spherical NPs or clusters.[58,59,63]

Our experiments have been performed under ambient conditions using an ICON-AFM apparatus controlled by a Nanoscope V electronics. The topographic images have been acquired in tapping mode, while the lift mode was used for the magnetic (MFM) imaging. The tip–sample distance has been determined by adding the mean topographic scan height (30 nm) to the tip-lift values used in the MFM scan. The spring constant of the used cantilevers was between 2 and 3 N m^{-1} and their resonance quality factor ranged between 500 and 1000. The probes were silicon tips covered with a hard magnetic coating presenting a coercive field of about 250 Oe. A magnetic field of 0.5 T was permanently applied in all experiments reported in this work. This field is high enough to saturate both the magnetic MFM probe and the NPs. Other details about the experiments are described in section SI3.† A characterization of the tip magnetic properties in the framework of the two-dipole model is presented in section SI4.† The magnetic moments of the NPs evaluated with the two-dipole model are in section SI5.†

The numerical simulations were conducted by considering the real geometry of the tip and the number and organization of the NPs. The configuration used in the simulations is sketched in Fig. SI9.† The advantage of our simulation model is that it considers a tip and a sample composed of small magnetic elements (meshes), which better account for the geometry of the systems. A magnetic moment corresponding to the respective volume is associated with each mesh element. Various mesh sizes have been checked, until a convergence was obtained. This typically corresponds to square meshes of lateral sizes below 2 nm (see section SI6†). The experimental

height of the tip H was also considered to obtain a convergence of the calculated force. The elementary force between two elementary magnetic elements of magnetic moments $\overrightarrow{M_1}$ and $\overrightarrow{M_2}$ separated by $\vec{r}$, reads:

$$\Delta\vec{F}\left(\overrightarrow{M_1},\overrightarrow{M_2},\vec{r}\right)=\frac{3\mu_0}{4\pi r^5}\left[\overrightarrow{M_2}\left(\overrightarrow{M_1}\cdot\vec{r}\right)+\overrightarrow{M_1}\left(\overrightarrow{M_2}\cdot\vec{r}\right)+\vec{r}\left(\overrightarrow{M_1}\cdot\overrightarrow{M_2}\right)-\frac{5\left(\overrightarrow{M_1}\cdot\vec{r}\right)\left(\overrightarrow{M_2}\cdot\vec{r}\right)}{r^2}\vec{r}\right]. \quad (2)$$

For a saturated magnetization along the z-direction, the total magnetic force is obtained by integrating over the whole system:

$$\vec{F}=\int \mathrm{d}\vec{r}'\mathrm{d}\vec{r}''\mathrm{d}\vec{F}\left(\overrightarrow{M_{\mathrm{NPs}}}(\vec{r}'),\overrightarrow{M_{\mathrm{Tip}}}(\vec{r}''),\vec{r}''-\vec{r}'\right), \quad (3)$$

where m represents the magnetization density. This expression can be numerically evaluated as a function of tip–sample distance z, yielding as well the first derivative of force *versus* distance, which can then be compared with the experimental phase shift. Section SI6† is a complete compilation of all parameters used in simulations.

3. Results and discussion

The high-temperature decomposition of magnetic precursors in organic solvents enables the formation of highly crystalline NPs of various sizes, shapes, compositions and magnetic properties.[10,64] Spherical Fe_3O_4 NPs with diameters of 30 nm ± 5 nm with high saturation magnetization values have been used (sections SI1 and SI2†). Prior to the deposition, the NPs were dispersed in chloroform. The residual traces of water in chloroform solvent lead to the assembly of NPs into ring structures of various diameters, as reported elsewhere for gold nanoparticles.[65] In between the ring structures, clusters comprising a different number of NPs can be found (Fig. 1, also section SI1†).

3.1. Magnetic phase-signals and the two-dipole model

Phase shift profiles as a function of tip–sample distance are shown in Fig. 1. The total magnetic moment of the clusters is

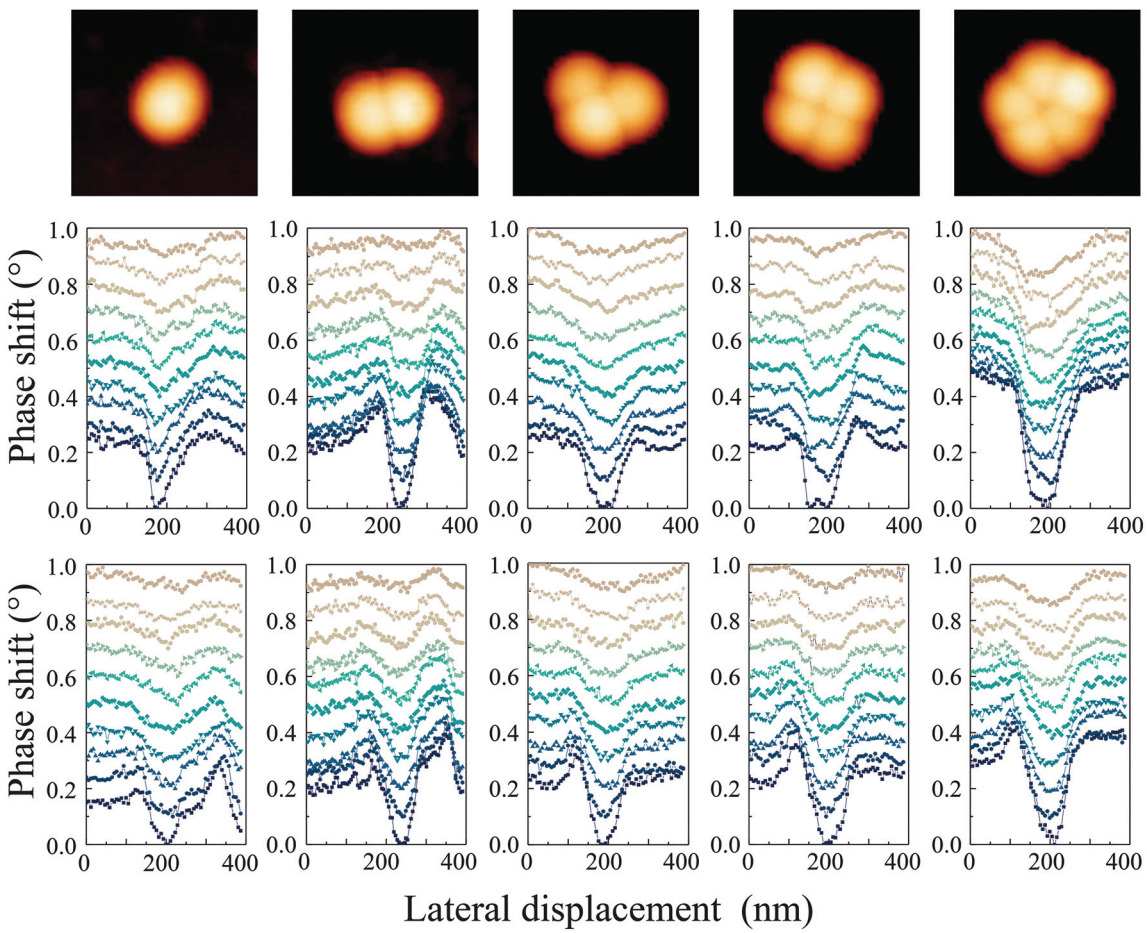

Fig. 1 Top row: AFM topographic images (200 × 200 nm^2) of a single NP and of various clusters made from two to five iron-oxide nanoparticles. The vertical scale bar is 34 nm. Middle row: MFM phase shift profiles (horizontal direction) as a function of tip–sample distance [tip lifts from 20 nm (dark blue) to 65 nm (light brown), values measured with respect to the topographic scan which is at about 30 nm from the sample surface]. Lower row: Phase shift profiles (vertical direction). Profiles are vertically offset for clarity.

expected to proportionally increase with the number of NPs composing the cluster, inducing a proportional increase of the phase shift as well. As seen in Fig. 1, this is not the case, since the variation of the phase shift signal does not scale with the number of NPs in the cluster. It is important to note that for large distances (80–95 nm: light-brownish curves), the phase signal tends, however, to vary proportionally with the number of NPs. We will see below that the phase shift also depends on the spatial arrangement of NPs in the cluster. In any case, the experimental results presented in Fig. 1 already justify a deeper analysis of how the magnetic field generated by different clusters evolves with the number and organization of NPs. Moreover, experimental observations also reveal the need to develop an accurate numerical model which can be subsequently used for quantitative characterization of the magnetic fields generated by the clusters of NPs.

3.2. Stray fields of single NPs

We have pursued our analysis by extracting quantitative information on the magnetic moments of various NP clusters. This was first realized by characterizing the MFM tip on reference samples consisting of six different isolated NPs having diameters ranging from 26 nm to 34 nm (Fig. 2 and Fig. SI5†). This analysis is a necessary step towards obtaining quantitative information about the magnetic moment of clusters.[58,59] It is worth noting that the diameters of the NPs have been estimated from height profiles and not from lateral sizes, as lateral dimensions are usually overestimated by tip convolution effects.[59] With the convolution effects not being present at the top of a nanoparticle, the extracted diameters of NPs are then in agreement with the size histograms obtained from electron microscopy images (section SI2†).

Another important issue in non-contact phase imaging is the electrostatic contributions which can interfere with "magnetic" phase shifts.[60] However, since all the measurements presented here are done in the saturation state of the magnetization, the electrostatic contribution is negligible as compared to the magnetic signal.[61] A negligible contribution of the electrostatic field is also indicated by the asymptotic variations of the phase signal with the tip–sample distance, which can only be explained by an insignificant gradient of the electrostatic field in the respective tip-distance interval.[62] The magnetic field produced by homogenously magnetized spherical NPs (especially at saturation) is hence well approximated to the field of a point dipole positioned at the center of the spherical NPs. This is the core of the two-dipole model as used in MFM, and is quite accurate for individual NPs.[62] The strength of the magnetic field is expected to be proportional to the magnetic moment of the nanoparticle, which in turn increases with its diameter (section SI4†).

Within this description, a slight deviation of the magnetic moment induces a significant modification of the field above the nanoparticles. Consequently, different volumes of the magnetic tip are involved in collecting the magnetic signal. Evolution of the MFM phase shift with the tip–sample distance is perfectly fitted with the two-dipole model, as seen in Fig. 2(a), provided that the magnetic dipole moment of the tip (m_{tip}) as well as its virtual location (δ_{tip}) within the tip volume are free fitting parameters. The significant variations with the NP diameter should be noted. Since the magnetic moment of each NP is well known, the two fitting parameters can be determined as a function of NP diameter. The resulting values are summarized in section SI4.† Those values are helpful for the subsequent analyses of clusters.

Each pair of parameters (m_{tip}, δ_{tip}) reflects the magnetic force field generated by an isolated NP. Both m_{tip} and δ_{tip} are found to increase with the increasing diameter of the particle. The values of m_{tip} are of the order of 10^{-17} Am^2, which is in good agreement with known values of magnetic moment of the tips. Plotting the m_{tip} as a function of δ_{tip} results in a linear dependence (Fig. 2). In our case, this dependence might be triggered by the reduced variation in the NP size, since for fields generated by nanoscale current-carrying parallel lithographed wires, a power-law behavior has been observed.[57]

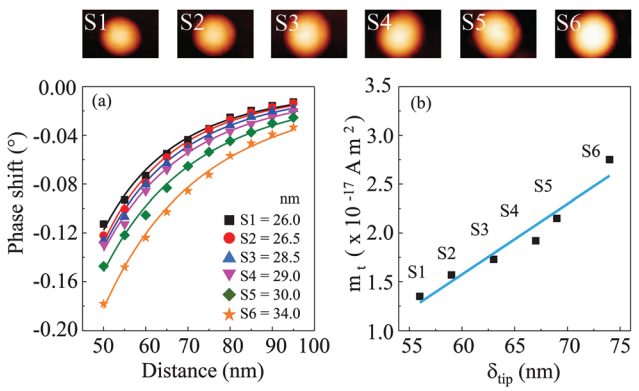

Fig. 2 (a) Phase shift of six single NPs of various diameters. Solid lines are fits obtained with the two-dipole model. The insets are the topographic images of the investigated NPs (150 × 80 nm^2). (b) Plot of the magnetic dipole moment of the tip as a function of its virtual location in the tip volume. The blue line is a linear fit.

3.3. Dimers and the role of planarity

The calibration of the magnetic tip enables the extraction of magnetic properties of clusters presenting different spatial organizations. For instance, clusters D1 and D2 in Fig. 3 were formed by assembling two NPs (D1: 30 nm and 28.5 nm; D2: 31 nm and 27.5 nm, respectively, also see Fig. SI6†). From these sizes, we can consider that both dimers have an identical volume of magnetic material even if their spatial arrangement is different. The main difference between the two dimers is that the NPs in D2 do not lie in the same surface plane. They partially overlap (section SI3†), appearing in the image in a more compact form than for D1 where both NPs are in the surface plane (Fig. 3).

It is now interesting to realize that the field generated by D2 emerges from a smaller area displaying a larger decay length. This is a simple and clear example of how the NPs in the dimer can impact the MFM signal along a particular direction. Moreover, the phase signal as a function of tip–sample dis-

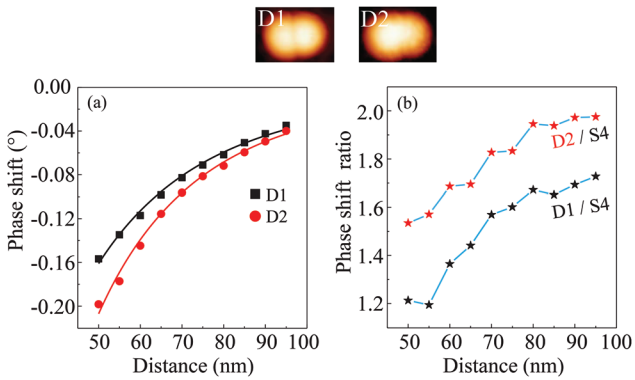

Fig. 3 (a) Phase shift of two dimers (D1 and D2) of different organizations. Solid lines are fits obtained with the two-dipole model. The insets are the topographic images of D1 and D2 (150 × 100 nm^2). (b) Distance dependence of the phase shift for the two dimers divided by the phase shift of a single NP.

tance (proportionally to the tip lift in MFM) of D2 exhibits a more sloped profile, which means that D2 generates a magnetic force field with a greater gradient magnitude in the normal direction.

In order to quantify the stray field generated by the clusters and to observe at which distances from the cluster surface the two-dipole model increases its accuracy we calculate the ratio between the phase signals of the clusters and of a single NP. As an example, the ratio between the experimental MFM phase shifts recorded for the two dimers (D1 and D2) and a single NP (S4) are shown in Fig. 3. The NP has been chosen in order to approach as close as possible the mean diameter of the NPs composing the cluster. As is seen, for distances above 80 nm, the D2/S4 ratio is indeed almost 2, in agreement with the two-dipole model (which stipulates that if the magnetic moment of the investigated cluster is doubled, the phase shift should also double). However, at lower distances, the ratio decreases down to about 1.5. The D1/S4 ratio starts at 1.7 at the largest distance and smoothly decreases towards 1.2 for the smallest distances [Fig. 3(b)], remaining therefore significantly lower than the ideal value of 2. These findings suggest in both cases that the tip does not perceive the entire cluster magnetic moment, which is a significant deviation from theory.

From the fits, δ_{tip} is 79 and 82 nm for D1 and D2, respectively. The δ_{tip} values are larger in comparison with the ones obtained for isolated NPs. By applying the linear dependence from Fig. 2(b), the values of magnetic moment of the tip are 2.95×10^{-17} Am^2 and 3.23×10^{-17} Am^2, when using D1 and D2, respectively. The higher value of the moment observed for D2 is due to the compact geometry, as the stray field interacts with a larger tip volume than in the case of D1. Finally, the extracted values of the magnetic dipole moment of D1 and D2 are 6.91×10^{-18} Am^2 and 7.69×10^{-18} Am^2, respectively. These values represent a percentage of 68.5% and 75.5% of the sum of magnetic moments of the two NPs forming D1 and D2. Consequently, when individual NPs come closer to each other and start clustering, only a fraction of the entire magnetic moment is detected by the MFM tip, undermining the two-dipole model. Interestingly, in compact geometries, where NPs partially overlay, the tip starts to perceive the entire magnetic moment for tip–sample distances exceeding roughly twice the diameter of a single NP.

3.4. Trimers, tetramers, and pentamers and compactness

It is pertinent to verify this trend and to further investigate the effect of the arrangement of NPs in clusters of higher order. The association of a third NP to a dimer leads to a variety of geometrical "trimer" configurations. We analyzed 5 different 3-fold clusters (trimers) (Fig. 4). In Tr1, a NP partially superimposes over the other two, giving rise to a slightly out-of-plane and compact triangular configuration when looking from above; Tr2 has an almost perfect isosceles in-plane triangular configuration, while Tr3 presents a slightly more open triangular shape. Tr4 is less bent, resembling a linear chain, whereas Tr5 has the two outer NPs in part overlaying the central one, forming a more compact geometry as seen from the top view. This has consequences for the field gradient generated in the out-of-plane direction, as discussed below in relation with the phase ratio comparison of the trimers.

As highlighted in Fig. 4(b), the phase shift for 3-fold clusters is even more drastically influenced by the NP arrangement. The evolution of the phase shift as a function of distance is very abrupt in the case of compact Tr1, *i.e.* the generated magnetic force field has the steepest gradient. The slope of the signal gradually decreases for Tr2 and Tr3, becoming the lowest for Tr4. In other words, as the trimers evolve from a compact triangular configuration to a linear-like chain, the magnitude of the generated magnetic force field decreases. In turn, the force field for Tr5 becomes again comparable to the one of Tr2 and Tr3, an effect which is due to the partial overlapping of outer NPs. Hence, we can conclude that the assemblage of NPs in linear-like chains generates reduced magnetic force fields above the center of the chain, whereas compact or overlapping NP geometries yield gradient fields of greater magnitudes.

The phase shift signals on the trimers have also been normalized by the phase signal of a single NP. Again, the latter

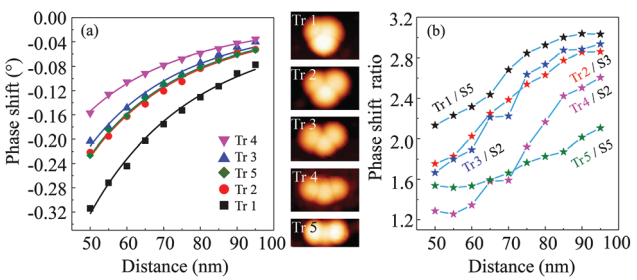

Fig. 4 (a) Phase shift of five 3-fold clusters (trimers) of various compactness. Solid lines are fits using the two-dipole model. The insets are the topographic images of the trimers Tr1 (scale bar: the large side of images is 170 nm). (b) Phase shifts for the five trimers divided by the phase shift of a single NP, reported as a function of tip–sample distance.

were estimated by averaging the diameters of the NPs constituting the respective trimers (Fig. SI7†). The magnetic moments of the trimers were evaluated by applying the same procedure as previously used for the dimers. Assuming for instance that the compact Tr1 trimer has a magnetic moment three times larger than the one of a single NP, it is expected that the phase shift ratio reaches a value of 3 over the entire range of distances. As shown in Fig. 4(b), the ratio is largely below 3 and only tends to this value for distances above 85 nm. For Tr1, the extracted magnetic moment almost equals the sum of the magnetic moments of the individual monomers – 90% recovery (section SI5†). In the case of Tr2 and Tr3 – where the apparent surface area increases as a result of the larger spacing of the NPs – the recovery percentages are 85.5% and 80%, respectively. The phase shift ratios for Tr2/S3 and Tr3/S2 are close to 3 only for large distances (85–95 nm), and steeply fall to 1.7 when the distance decreases to 50 nm [Fig. 4(b)]. The recovery percentage reduces significantly to 66% and 70% for Tr4 and Tr5 clusters, respectively. Accordingly, the Tr4/S2 ratio varies very rapidly from 1.3 to 2.6, while the Tr5/S5 ratio has a smooth linear trend between 1.5 and 2.

The magnitude of the detected magnetic moment of a cluster therefore significantly depends on the degree of compactness and on the tip–sample distance. For compact triangular clusters the tip detects a full magnetic moment only at distances exceeding 80 nm. As the separation between NPs increases, the recorded magnetic force field decreases, affecting the overall magnitude of the magnetic moment of clusters.

We have expanded our study to larger clusters formed by the assembly of four and five NPs. In the case of "tetramers" (Te), the NPs are spatially arranged in such a way that they are located in the corner of a slightly distorted square, while NPs in "pentamers" (Pe) form an almost regular pentagon (Fig. 5 & Fig. SI7†). The phase shift of the pentamer has a slightly larger magnitude than that given by the tetramer (Fig. SI8†). In general, we find that the less compact geometries have a great impact on the magnitude of the extracted magnetic moment. The recovery percentage is 64% and 67% for the tetramer and pentamer, respectively (Table SI2†). This indicates that a larger 2D spatial extension of NPs results in a magnetic force field of a smaller magnitude and a shorter decay length. As can be seen in Fig. 5, where phase shift ratios are plotted for clusters with increasing connectivity, the Te/S4 and Pe/S4 phase shift ratios only approach values of 3.5 and 4.6, respectively, at the largest distances. Only the smaller compact clusters have the tendency to reach a phase shift ratio identical to the number of NPs. These findings again cannot be understood in the framework of the two-dipole model where the clusters are described by point-like magnetic dipole moments.

4. Numerical simulations

Calculations of the magnetostatic interactions between the microscope tip and the NPs were modeled by using the configurations found experimentally. A detailed description of the method can be found in section SI6.† The interaction between the magnetic tip and the sample has been simulated by placing the tip apex above the center of mass of the studied clusters. In Fig. 6(a), we show the computed magnetic forces as a function of distance for three isolated NPs of different diameters: D = 26 nm, 30 nm and 34 nm. As expected, the magnetic force increases with the size of the NPs while the total magnetic moment scales with the volume. In Fig. 6(b), the theoretical force gradient values are plotted (which are proportional to the experimental phase shift) with respect to the tip–sample distance. Comparison with the experimental

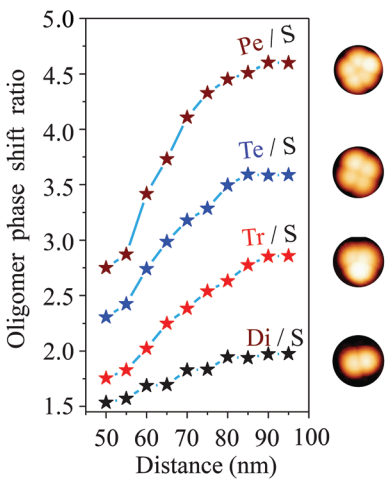

Fig. 5 Phase shift of several clusters divided by the phase shift of a single NP. The NP has been chosen with a diameter close to the mean diameter of those composing the cluster. The insets are the topographic images of the analyzed clusters.

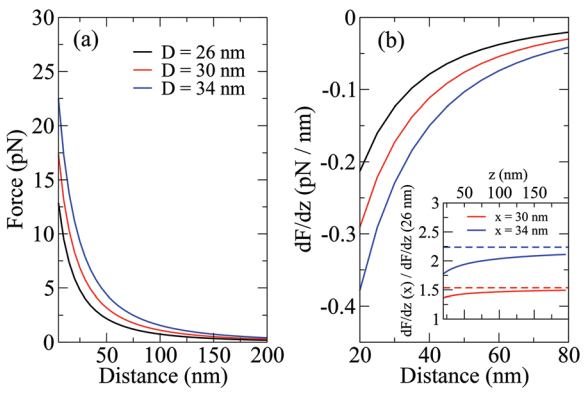

Fig. 6 (a) Variation of the magnetic force between the tip and three single NPs of different diameters (D = 26 nm, 30 nm and 34 nm) as a function of tip–NP distance. (b) Variation of the force gradient as a function of distance for the three different single NPs. The inset exhibits the variation of the gradient force ratio between the larger single NPs (D = 30 and 34 nm) and the smallest single NP (D = 26 nm) as a function of distance by using our simulation method (full curve) and an equivalent two-dipole model (dashed curve).

results presented in Fig. 2 reveals that the simulated force gradients exhibit the same trend as in experiments. Indeed, in both simulated and experimental cases, the force gradient increases for larger NPs. The difference between the force gradients however shrinks as the distance between the tip and the NP increases.

Due to the finite element modeling used here, the numerical analyses do not need to take into account a change in the tip magnetization or any modification in the localization of tip moment, as required in the two-dipole model. Deviations from the two-dipole model can be quantified by comparing the simulated force gradient ratio between two different NPs with respect to the two-dipole model. In the latter case, the force gradient ratio between two different NPs is constant as a function of distance, as shown for instance in the inset of Fig. 6(b). The simulations indicate that the ratios depend on the tip–sample distance, progressively converging to the value given by the two-dipole model. The simulations are therefore expected to give details about why the fitting of experimental phase shifts with the two-dipole model required a change of both the tip magnetic moment and its location within the tip volume.

4.1. Influence of compactness

To study the influence of the in-plane compactness of the clusters on the generated magnetic field, we calculated the force gradients for four configurations where the in-plane arrangement of the NPs has been changed. Since the most relevant experimental results concerning the modification of the magnetic force field have been obtained on 3-fold clusters, we chose to work with clusters formed by NPs of the same diameter (D = 30 nm). Their configurations are shown in Fig. 7. The 3-fold clusters can be differentiated by the parameter θ which represents the angle between the central NP and the two outer NPs [Fig. 7(c)]. The first trimer has a linear-like chain configuration, which corresponds to an angle $\theta = 0$. In the next two configurations, the outer NPs are symmetrically displaced with respect to the central NP, while keeping the NPs in the same plane, *i.e.* the one perpendicular to the tip axis. This gives rise to triangular clusters with $\theta = \pi/8$ and $\theta = \pi/4$, respectively. The latter cluster has a more compact structure with the three NPs forming an equilateral triangle $\theta = \pi/3$.

From Fig. 7(a), it can be seen that the magnetic force exerted on the tip gradually increases as the cluster changes from a linear to a triangular configuration. The differences between the four configurations are as expected more visible at small distances. The more compact the trimer, the stronger the magnetic force. The magnitude of the magnetic force field therefore depends on the geometrical configuration of the trimer. The slope of the force gradient *vs.* distance is also significantly reduced for low compactness [Fig. 7(b)]. The computed force gradients are consequently in very good agreement with the experimental phase shifts plotted in Fig. 4. Moreover, at large distances ($\gg D$), the force gradients converge to the same value because all four computed configurations have the same total magnetic moment. In the case of the most compact

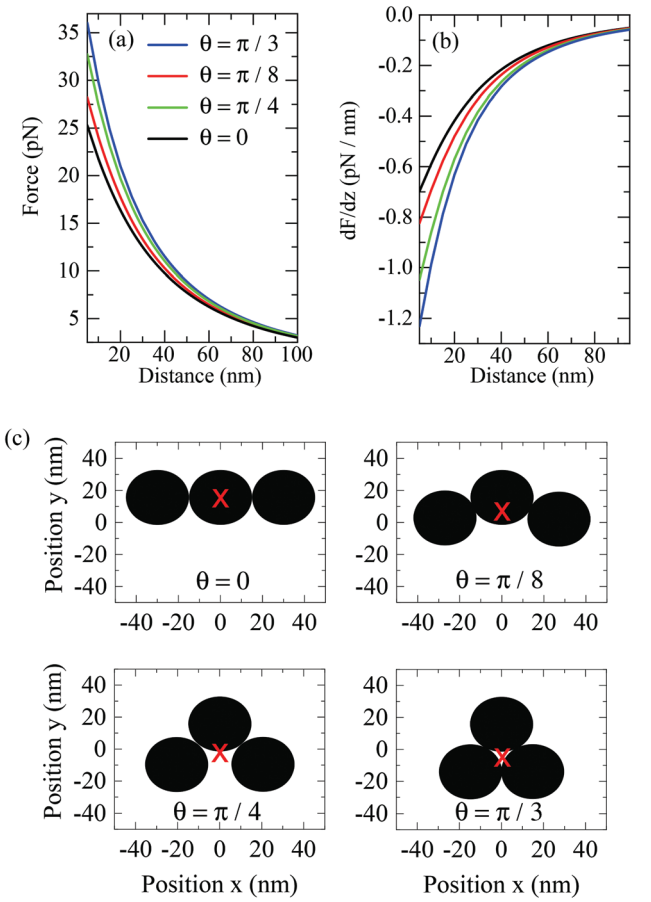

Fig. 7 (a) Force and (b) force gradient between the tip and the four clusters depicted in (c). (c) Top view of four trimers of different compactness. The red crosses represent the lateral position of the tip.

trimer ($\theta = \pi/3$), the force gradient shows the greatest variation, as also found experimentally (Tr1 in Fig. 4).

The force gradients shown in Fig. 7(b) are divided by the force gradient obtained for a single NP. The resulting curves are shown with solid lines in Fig. 8(a). It is seen that the ratios display a smoother variation as the trimers adopt a less compact geometry. It is worth recalling that these ratios indicate how the magnetic fields generated by a cluster deviate from the fields generated by a single NP. As a matter of fact, the ratio cannot be larger than three for a trimer.

When the Tr/S ratio reaches the maximal value of three, it means that the magnetic force field is not any more dependent on the spatial arrangement in the trimer. In our numerical analyses, we found a maximum value of 2.8 at 95 nm in the case of the most compact trimer ($\theta = \pi/3$). This maximum value decreases considerably at the same distance for less compact trimers. It means that even at distances larger than 2–3 times the NP diameter, the tip is still sensitive to the 2D spatial arrangement of the NPs in the trimer.

For the sake of comparison, we also calculated the force gradient ratios for $\theta = 0$ and $\theta = \pi/3$ trimers using the two-dipole model. The results are shown with dashed lines in

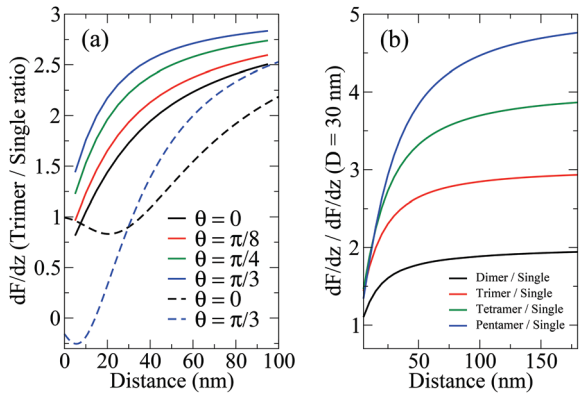

Fig. 8 (a) Force gradients for the four trimers divided by the force gradient of a single NP (30 nm in diameter). For comparison, the results for $\theta = 0$ and $\theta = \pi/3$ as computed with the two-dipole model are shown with dashed lines. (b) Force gradients for clusters composed from two to five NPs divided by the force gradient of a NP.

Fig. 8(a). A full analysis performed with the two-dipole model is presented in section SI7.† At large distances >2*D*, the ratio for the compact trimer is greater than the ratio of the linear trimer, which is qualitatively in agreement with both previous simulations and experiments. For small distances (<2*D*), the ratios show a completely different variation as compared with the respective curves obtained with our finite element model and with the experiments. For instance, at distances of the order of *D*, the two dipole model predicts a ratio for the linear-like chain cluster higher than the one for the compact trimer, an aspect which is neither observed in our finite-element modeling nor in the experiments. The ratio even becomes negative at very short distances (<*D*), meaning that the force between the tip and clusters is attractive. This happens because the tip dipole moment is so close to the dipole moment of NPs that there is an angle where the sign of the magnetic force changes. This is not the case either in our finite element modeling or in the experiments, because of the finite size of the NPs and of the tip. Altogether, these results already show that the two-dipole model cannot capture a reliable magnetostatic interaction at separation distances <2*D*.

The force gradients of several clusters ranging from two to five NPs divided by the force gradient of a single NP are shown in Fig. 8(b). These theoretical ratios can be compared with the experimental curves presented in Fig. 5. As is seen, the numerical results support the experimental findings. Depending on the number of NPs composing the clusters, the ratios progressively increase as the distance increases, approaching a saturation value. Above approximately 70 nm, the ratios are almost 2 and 3 for dimers and trimers, respectively. Instead, at the same 70 nm separation distance, the ratios for tetramers and pentamers are only 3.6 and 4.5, saturating at 3.9 and 4.8 only for very large distances. This is due to the fact that the tip senses differently the magnetic force fields depending on the 2D organization of the NPs in the cluster, as also observed experimentally.

5. Summary and conclusions

We presented a combined experimental and theoretical study on a quantitative evaluation of the magnetic force fields generated by clusters formed by associations of single NPs on a solid non-magnetic substrate. The experimental results obtained under a saturation magnetic field of 0.5 T have shown that the magnetic force fields do not increase proportionally with the number of NPs in the clusters. Furthermore, for dimeric and trimeric clusters, minute modifications of the 2D spatial arrangement of NPs in the clusters drastically modify the surrounding magnetic field. For these clusters, the magnitude of the generated force field follows the prediction of the two-dipole model, but only at distances exceeding some critical values (about twice the diameter of a NP). For tetramers and pentamers the two-dipole model is found to overestimate the value of the magnetic moments in the whole range of the experimental distances. The largest the in-plane lateral expansion of the cluster the less accurate is the two-dipole model in extracting quantitative information. This is because the principal condition for the use of a two-dipole model is related to the lateral extension of the clusters which should be smaller than the distance at which the magnetic force field is evaluated.

Good agreement with the experimental results, in the entire range of tip–sample distances, was obtained by considering the real geometry of the system, namely by splitting both the tip and sample in a finite number of microscopic elements and performing a full pairwise integration of magnetostatic potentials. The numerical calculations conducted with this finite-element model provided unprecedented insight into the quantitative evaluation of the magnetic field generated by assemblies of NPs, and put forward the importance of the spatial organization. The magnetic force field in the proximity of clusters has a complex distance-dependent structure, being driven significantly by the exact number of NPs. Compact clusters have a general tendency to generate an enhanced force field able to extend at larger distances, which is the result of interparticle magnetic interactions and cooperative effects. Our results may have an impact on the chemical design of NP-based clusters for various applications, including biomedical and therapeutic strategies or magnetic information technologies.

Conflicts of interest

There are no conflicts to declare.

Acknowledgements

We thank N. Beyer for technical assistance, O. Ersen for TEM measurements, S. Colis for magnetic hysteresis measurements, and R. Dudric for XRD data. This work is supported by ANR METABIP (12 BS10 003 01), ANR OH-RISQUE SMARAGD (14

OHRI 0008 01), EOARD (FA8655-13-1-3001) and partially by ANR-11-LABX-0058-NIE within the Investissement d'Avenir program ANR-10-IDEX-0002-02. C. Iacovita acknowledges financial support from Romanian National Authority for Scientific Research, CNCSIS-UEFISCDI, through researcher mobility project no. PN-III-P1-1.1-MC-2017-0981 and a research project to stimulate young independent teams with no. PN-III-P1-1.1-TE-2016-0967. We thank CNRS & University of Strasbourg for support.

References

1 S. Laurent, D. Forge, M. Port, A. Roch, C. Robic, L. Vander Elst and R. N. Muller, *Chem. Rev.*, 2008, **108**, 2064–2110.
2 J. Gao, H. Gu and B. Xu, *Acc. Chem. Res.*, 2009, **42**, 1097–1107.
3 N. Lee, H. R. Cho, M. H. Oh, S. H. Lee, K. Kim, B. H. Kim, K. Shin, T.-Y. Ahn, J. W. Choi, Y.-W. Kim, S. H. Choi and T. Hyeon, *J. Am. Chem. Soc.*, 2012, **134**, 10309–10312.
4 M. Colombo, S. Carregal-Romero, M. F. Casula, L. Gutiérrez, M. P. Morales, I. B. Böhm, J. T. Heverhagen, D. Prosperi and W. J. Parak, *Chem. Soc. Rev.*, 2012, **41**, 4306.
5 A.-H. Lu, E. L. Salabas and F. Schüth, *Angew. Chem., Int. Ed.*, 2007, **46**, 1222–1244.
6 J. H. Kang, E. Um, A. Diaz, H. Driscoll, M. J. Rodas, K. Domansky, A. L. Watters, M. Super, H. A. Stone and D. E. Ingber, *Small*, 2015, **11**, 5657–5666.
7 M. Mahmoudi, S. Sant, B. Wang, S. Laurent and T. Sen, *Adv. Drug Delivery Rev.*, 2011, **63**, 24–46.
8 W. Wu, Z. Wu, T. Yu, C. Jiang and W.-S. Kim, *Sci. Technol. Adv. Mater.*, 2015, **16**, 023501.
9 D. Ling and T. Hyeon, *Small*, 2013, **9**, 1450–1466.
10 A. Demortire, P. Panissod, B. P. Pichon, G. Pourroy, D. Guillon, B. Donnio and S. Bégin-Colin, *Nanoscale*, 2011, **3**, 225–232.
11 S. Noh, W. Na, J. Jang, J.-H. Lee, E. J. Lee, S. H. Moon, Y. Lim, J.-S. Shin and J. Cheon, *Nano Lett.*, 2012, **12**, 3716–3721.
12 U. O. Häfeli, J. S. Riffle, L. Harris-Shekhawat, A. Carmichael-Baranauskas, F. Mark, J. P. Dailey and D. Bardenstein, *Mol. Pharm.*, 2009, **6**, 1417–1428.
13 G. Liu, J. Gao, H. Ai and X. Chen, *Small*, 2013, **9**, 1533–1545.
14 H. Bin Na, I. C. Song and T. Hyeon, *Adv. Mater.*, 2009, **21**, 2133–2148.
15 Z. R. Stephen, F. M. Kievit and M. Zhang, *Mater. Today*, 2011, **14**, 330–338.
16 N. Lee and T. Hyeon, *Chem. Soc. Rev.*, 2012, **41**, 2575–2589.
17 Y. Jun, J. Lee and J. Cheon, *Angew. Chem., Int. Ed.*, 2008, **47**, 5122–5135.
18 L. Lartigue, C. Innocenti, T. Kalaivani, A. Awwad, M. del M. Sanchez Duque, Y. Guari, J. Larionova, C. Guerin, J.-L. G. Montero, V. Barragan-Montero, P. Arosio, A. Lascialfari, D. Gatteschi and C. Sangregorio, *J. Am. Chem. Soc.*, 2011, **133**, 10459–10472.
19 L. C. Branquinho, M. S. Carriao, A. S. Costa, N. Zufelato, M. H. Sousa, R. Miotto, R. Ivkov and A. F. Bakuzis, *Sci. Rep.*, 2013, **3**, 2887.
20 C. Martinez-Boubeta, K. Simeonidis, A. Makridis, M. Angelakeris, O. Iglesias, P. Guardia, A. Cabot, L. Yedra, S. Estradé, F. Peiro, Z. Saghi, P. A. Midgley, I. Conde-Leborán, D. Serantes and D. Baldomir, *Sci. Rep.*, 2013, **3**, 1652.
21 C. Blanco-Andujar, A. Walter, G. Cotin, C. Bordeianu, D. Mertz, D. Felder-Flesch and S. Begin-Colin, *Nanomedicine*, 2016, **11**, 1889–1910.
22 O. Veiseh, J. W. Gunn and M. Zhang, *Adv. Drug Delivery Rev.*, 2010, **62**, 284–304.
23 M. Das, D. Mishra, P. Dhak, S. Gupta, T. K. Maiti, A. Basak and P. Pramanik, *Small*, 2009, **5**, 2883–2893.
24 E. Bellido, N. Domingo, I. Ojea-Jiménez and D. Ruiz-Molina, *Small*, 2012, **8**, 1465–1491.
25 A. Shavel, B. Rodriguez-González, M. Spasova, M. Farle and L. Liz-Marzán, *Adv. Funct. Mater.*, 2007, **17**, 3870–3876.
26 L. Balcells, I. Stankovic, Z. Konstantinovic, A. Alagh, V. Fuentes, L. López-Mir, J. Oró, N. Mestres, C. Garcia, A. Pomar and B. Martinez, *Nanoscale*, 2019, **11**, 14194–14202.
27 J. M. Perez, L. Josephson, T. O'Loughlin, D. Högemann and R. Weissleder, *Nat. Biotechnol.*, 2002, **20**, 816–820.
28 C. Min, H. Shao, M. Liong, T.-J. Yoon, R. Weissleder and H. Lee, *ACS Nano*, 2012, **6**, 6821–6828.
29 J. Conde, J. T. Dias, V. Grazão, M. Moros, P. V. Baptista and J. M. de la Fuente, *Front. Chem.*, 2014, **2**, 48.
30 L. Gutiérrez, L. de la Cueva, M. Moros, E. Mazaro, S. de Bernardo, J. M. de la Fuente, M. P. Morales and G. Salas, *Nanotechnology*, 2019, **30**, 112001.
31 K. Wu, K. Schliep, X. Zhang, J. Liu, B. Ma and J.-P. Wang, *Small*, 2017, **13**, 1604135.
32 P. Gillis and S. H. Koenig, *Magn. Reson. Med.*, 1987, **5**, 323–345.
33 L. Josephson, J. M. Perez and R. Weissleder, *Angew. Chem., Int. Ed.*, 2001, **40**, 3204–3206.
34 R. A. Brooks, *Magn. Reson. Med.*, 2002, **47**, 388–391.
35 H. Shao, T.-J. Yoon, M. Liong, R. Weissleder and H. Lee, *Beilstein J. Nanotechnol.*, 2010, **1**, 142–154.
36 H. Gavilán, A. Kowalski, D. Heinke, A. Sugunan, J. Sommertune, M. Varón, L. K. Bogart, O. Posth, L. Zeng, D. González-Alonso, C. Balceris, J. Fock, E. Wetterskog, C. Frandsen, N. Gehrke, C. Grüttner, A. Fornara, F. Ludwig, S. Veintemillas-Verdaguer, C. Johansson and M. P. Morales, *Part. Part. Syst. Charact.*, 2017, **34**, 1700094.
37 P. Bender, J. Fock, C. Frandsen, M. F. Hansen, C. Balceris, F. Ludwig, O. Posth, E. Wetterskog, L. K. Bogart, P. Southern, W. Szczerba, L. Zeng, K. Witte, C. Grüttner, F. Westphal, D. Honecker, D. González-Alonso, L. F. Barquin and C. Johansson, *J. Phys. Chem. C*, 2018, **122**, 3068.
38 S. Ota, Y. Matsugi, T. Nakamura, R. Takeda, Y. Takemura, I. Kato, S. Nohara, T. Sasayama, T. Yoshida and K. Enpuku, *J. Magn. Magn. Mater.*, 2019, **474**, 311.

39 P. Grütter, H. J. Mamin and D. Rugar, *Magnetic force microscopy*, Springer, Berlin, Heidelberg, 1992, pp. 151–207.
40 R. E. Dunin-Borkowski, T. Kasama, A. Wei, S. L. Tripp, M. J. Hÿtch, E. Snoeck, R. J. Harrison and A. Putnis, *Microsc. Res. Tech.*, 2004, **64**, 390–402.
41 I. Passeri, D. Angeloni, L. Reggente and M. Rossi, *Magnetic Force Microscopy, Magnetic Characterization Techniques for Nanomaterials*, Springer Berlin Heidelberg, Berlin, Heidelberg, 2017.
42 P. Ares, M. Jaafar, A. Gil, J. Gómez-Herrero and A. Asenjo, *Small*, 2015, **11**, 4731–4736.
43 C. Dietz, E. T. Herruzo, J. R. Lozano and R. Garcia, *Nanotechnology*, 2011, **22**, 125708.
44 A. Krivcov, J. Schneider, T. Junkers and H. Möbius, *Phys. Status Solidi A*, 2018, **216**, 1800753.
45 M. V. Rastei, R. Meckenstock, J. P. Bucher, E. Devaux and T. Ebbesen, *Appl. Phys. Lett.*, 2004, **85**, 2050–2052.
46 M. V. Rastei, R. Meckenstock and J. P. Bucher, *Appl. Phys. Lett.*, 2005, **87**, 222505.
47 M. V. Rastei, M. Abes, J. P. Bucher, A. Dinia and V. Pierron-Bohnes, *J. Appl. Phys.*, 2006, **99**, 084316.
48 H. J. Hug, B. Stiefel, P. J. A. van Schendel, A. Moser, R. Hofer, S. Martin, H.-J. Güntherodt, S. Porthun, L. Abelmann, J. C. Lodder, G. Bochi and R. C. O'Handley, *J. Appl. Phys.*, 1998, **83**, 5609–5620.
49 P. J. A. van Schendel, H. J. Hug, B. Stiefel, S. Martin and H.-J. Güntherodt, *J. Appl. Phys.*, 2000, **88**, 435–445.
50 T. Häberle, F. Haering, H. Pfeifer, L. Han, B. Kuerbanjiang, U. Wiedwald, U. Herr and B. Koslowski, *New J. Phys.*, 2012, **14**, 043044.
51 S. Schreiber, M. Savla, D. V. Pelekhov, D. F. Iscru, C. Selcu, P. C. Hammel and G. Agarwal, *Small*, 2008, **4**, 270–278.
52 U. Hartmann, *Phys. Lett. A*, 1989, **137**, 475–478.
53 R. B. Proksch, T. E. Schäffer, B. M. Moskowitz, E. D. Dahlberg, D. A. Bazylinski and R. B. Frankel, *Appl. Phys. Lett.*, 1995, **66**, 2582–2584.
54 M. Abes, M. V. Rastei, J. Venuat, A. Carvalho, S. Boukari, E. Beaurepaire, P. Panissod, A. Dinia, J. P. Bucher and V. Pierron-Bohnes, *J. Appl. Phys.*, 2009, **105**, 113916.
55 D. Passeri, C. Dong, M. Reggente, L. Angeloni, M. Barteri, F. A. Scaramuzzo, F. De Angelis, F. Marinelli, F. Antonelli, F. Rinaldi, C. Marianecci, M. Carafa, A. Sorbo, D. Sordi, I. W. Arends and M. Rossi, *Biomatter*, 2014, **4**, e29507.
56 J. Lohau, S. Kirsch, A. Carl, G. Dumpich and E. F. Wassermann, *J. Appl. Phys.*, 1999, **86**, 3410–3417.
57 T. Kebe and A. Carl, *J. Appl. Phys.*, 2004, **95**, 775–792.
58 S. Sievers, K.-F. Braun, D. Eberbeck, S. Gustafsson, E. Olsson, H. W. Schumacher and U. Siegner, *Small*, 2012, **8**, 2675–2679.
59 L. Angeloni, D. Passeri, S. Corsetti, D. Peddis, D. Mantovani and M. Rossi, *Nanoscale*, 2017, **9**, 18000–18011.
60 M. Jaafar, O. Iglesias-Freire, L. Serrano-Ramon, M. Ricardo Ibarra, J. Maria de Teresa and A. Asenjo, *Beilstein J. Nanotechnol.*, 2011, **2**, 552–560.
61 L. Angeloni, D. Passeri, F. A. Scaramuzzo, D. Di Iorio, M. Barteri, D. Mantovani and M. Rossi, *AIP Conf. Proc.*, 2016, **1749**, 020006.
62 L. Angeloni, D. Passeri, M. Reggente, D. Mantovani and M. Rossi, *Sci. Rep.*, 2016, **6**, 26293.
63 C. Moya, Ó. Iglesias-Freire, X. Batlle, A. Labarta and A. Asenjo, *Nanoscale*, 2015, **7**, 17764–17770.
64 L. Wu, A. Mendoza-Garcia, Q. Li and S. Sun, *Chem. Rev.*, 2016, **116**, 10473–10512.
65 L. Malassis, D. Jishkariani, C. B. Murray and B. Donnio, *Nanoscale*, 2016, **8**, 13192–13198.